# Measurement Report: Elevated atmospheric ammonia may promote the particle pH and HONO formation: Insights from the COVID-19 pandemic

Xinyuan Zhang[1,2], Lingling Wang[3], Nan Wang[3], Shuangliang Ma[3], Shenbo Wang[2,4 *], Ruiqin Zhang[2,4**], Dong Zhang[1,2], Mingkai Wang[2,4], Hongyu Zhang[1,2].

[1] College of Chemistry, Zhengzhou University, Zhengzhou, 450000, China

[2] Research Institute of Environmental Sciences, Zhengzhou University, Zhengzhou 450000, China

[3] Henan Provincial Ecological Environment Monitoring and Safety Center, Zhengzhou, 450000, China

[4] School of Ecology and Environment, Zhengzhou University, Zhengzhou, 450000, China

**Correspondence:** Shenbo Wang (shbwang@zzu.edu.cn) and Ruiqin Zhang (rqzhang@zzu.edu.cn)

## Abstract

HONO plays a crucial role as a precursor to OH radicals in the tropospheric atmosphere. The incongruity between HONO concentration and $NO_x$ emissions during the COVID-19 pandemic remains puzzling. Here, we show evidence from field observations of ten sites in China that there was a noticeable increase in $NH_3$ concentrations during the COVID-19 pandemic. In addition to the meteorological conditions, the significant decrease in sulfate and nitrate concentrations enhanced the portioning of $NH_4^+$ to $NH_3$. Sensitivity analysis indicated that the decrease in anion concentrations (especially sulfate and nitrate) and the increase in cation concentrations during the COVID-19 pandemic led to an increase in particle pH. In other words, the excess ammonia determined the promoting pH. The calculation of reaction rates indicates that during the epidemic, the increase in pH may promote the generation of HONO by facilitating redox reactions, which highlights the importance of coordinating the control of $SO_2$, $NO_x$, and $NH_3$ emissions.

**Keywords:** Ammonia, HONO, Gas-particle portioning, Acidity, COVID-19 pandemic

# 1. Introduction

Nitrous acid (HONO) is a critical precursor of hydroxyl radical (OH), contributing to more than 60% of OH production (Alicke, 2003;Platt et al., 1980;Kleffmann et al., 2005). The OH can react with carbon monoxide, nitrogen oxides ($NO_x$), sulfur dioxide ($SO_2$), and volatile organic compounds to produce secondary pollutants such as ozone ($O_3$) and $PM_{2.5}$ (particulate matter with an aerodynamic diameter less than or equal to 2.5 μm), thereby affecting air quality, human health, and global climate change (Li et al., 2021a;Wang et al., 2023b;Lu et al., 2018)

High concentrations of HONO are present in urban daytime atmospheres, and exploring its sources has become a hot and challenging topic in the field of atmospheric chemistry (Jiang et al., 2022;Xu et al., 2019). Various sources of atmospheric HONO have been identified, including combustion processes (e.g., vehicle emissions) (Kramer et al., 2020;Liao et al., 2021a;Li et al., 2021b), direct emissions from soil (Su and Zhang, 2011;Oswald et al., 2013;Meusel et al., 2018), homogeneous reactions between NO and OH radicals (Pagsberg, 1997;Atkinson and Rossi, 2004), heterogeneous reactions of $NO_2$ on aerosols and ground surfaces (Zhang et al., 2020a;McFall et al., 2018;Liu et al., 2014;Liu et al., 2020a), and photolysis of nitrate (Spataro and Ianniello, 2014;Scharko et al., 2014;Romer et al., 2018;Ye et al., 2017;Shi et al., 2021). During the pandemic control periods, there was a substantial reduction in vehicle traffic flow and industrial emissions, leading to a decrease of more than 60% in $NO_x$ emissions in eastern China (Huang et al., 2021a). It was initially expected that the concentration of HONO would also decrease proportionally. However, Liu et al. (2020b) observed that the decrease in

HONO concentration during the pandemic period was only 31% (from 1.5 ppb to 0.9 ppb), which was significantly lower than the reductions in NO (62%, from 26.3 to 4.2 ppb) and $NO_2$ (36%, from 15.5 to 6.2 ppb). Furthermore, the observed concentrations of HONO during the COVID-19 pandemic in 2020 were higher than those during the corresponding period in 2021 in Beijing (Luo et al., 2023). These findings suggest the existence of a considerable unknown source of HONO during the COVID-19 pandemic period.

Ammonia ($NH_3$) is a primary alkaline gas in the atmosphere, capable of influencing the pH level of particulate matter and plays a crucial role in the atmospheric nitrogen cycle (Gu et al., 2022;Xu et al., 2020;Gong et al., 2011). Several studies have indicated that $NH_3$ can promote the formation of HONO by promoting the hydrolysis of $NO_2$ (Xu et al., 2019) or the redox reaction of $NO_2$ with $SO_2$ (Liu et al., 2023). Moreover, previous studies have reported that $NH_3$ concentrations in the atmosphere, particularly in rural areas, significantly increased during the pandemic (Xu et al., 2022). Consequently, the rise in $NH_3$ may contribute to the enhanced formation of HONO (Huang et al., 2021a). Unfortunately, there is currently a lack of research on the relationship between enhanced $NH_3$ and HONO during the COVID-19 pandemic period.

To address this, online observational data on the chemical composition of $PM_{2.5}$, gaseous pollutants, and meteorological conditions at ten sites in China before and during the COVID-19 pandemic period were analyzed to investigate the variation in $NH_3$ concentrations and particle pH, and explore the promoting effect of increased pH values on HONO formation.

## 2. Materials and methods

### 2.1 Observation sites

Online measurements were conducted at four urban and six rural sites in Henan Province, China from January 1 to February 29, 2020, including Sanmenxia (U-SMX), Zhoukou (U-ZK), Zhumadian (U-ZMD), and Xinyang (U-XY), as well as rural locations including Anyang (R-AY), Xinxiang (R-XX), Jiaozuo (R-JZ), Shangqiu (R-SQ), Nanyang (R-NY), and Puyang (R-PY). Descriptions and the spatial distribution of these ten sites can be found in Table S1 and Fig. S1.

### 2.2 Measurements

The aerosol and gas monitor (MARGA, Metrohm, Switzerland) was used to analyze the hourly water-soluble ions ($Na^+$, $NH_4^+$, $K^+$, $Mg^{2+}$, $Ca^{2+}$, $Cl^-$, $NO_3^-$, and $SO_4^{2-}$) in $PM_{2.5}$, as well as gaseous species ($NH_3$, $HNO_3$, HCl, and HONO) at ten sampling sites. The MARGA instrument is widely used (Chen et al., 2017;Stieger et al., 2019;Twigg et al., 2022). A detailed description of the instrument and QA/QC can be found in Text S1. In brief, the atmospheric sample passes through a $PM_{2.5}$ cut-off head, and both particles and gases enter a wet rotating dissolution device for diffusion. Subsequently, the particles in the sample undergo hygroscopic growth and condensation in an aerosol supersaturated vapor generator, followed by collection and ion chromatographic analysis. The gases in the sample are oxidized by $H_2O_2$ in the dissolution device, absorbed into a liquid solvent, and then entered the gas sample collection chamber for ion chromatographic quantification. The range of minimum detection limits for water-soluble ions was between 0.002 μg/m$^3$ ($Cl^-$) to 0.081 μg/m$^3$ ($NH_4^+$). Uncertainties of 20% are assumed for the detection of $NH_3$ and $NH_4^+$, while uncertainties of 10% are assumed for other components (Wang et al., 2020;Wang et al., 2022). In addition, a detailed description of HONO measurement using this system can be found in Text S2. Overall, the limit of detection for HONO was 4 pptv and the uncertainty was estimated to be ± 20%.

The data for $NO_2$ and $SO_2$ were obtained from a series of instruments provided by Thermo Fisher Scientific (USA). The hourly concentrations of organic carbon (OC) in $PM_{2.5}$ were analyzed using a carbon analyzer (Model 4, Sunset Laboratory., USA). Detailed descriptions of the $NO_2$, $SO_2$, and carbon analyzers can be found in Text S3. The smart weather stations (LUFFTWS500, Sutron, Germany) were utilized for synchronized observation of meteorological parameters including pressure, temperature (T), and relative humidity (RH).

## 2.3 Data analysis.

### 2.3.1 pH prediction.

The thermodynamic model ISORROPIA-II was used to estimate the pH value of the particles (Fountoukis, 2007) by inputting RH, T, $K^+$, $Ca^{2+}$, $Mg^{2+}$, total ammonia ($TNH_x = 17 \times (\frac{[NH_4^+]}{18} + \frac{[NH_3]}{17})$), total sulfuric acid ($TH_2SO_4$, $SO_4^{2-}$), total sodium (TNa, $Na^+$), total chlorine (TCl, $Cl^-$), and total nitrate ($TNO_3 = NO_3^- + HNO_3$). The model has two calculation modes: the forward mode and reverse mode, and the aerosol dissolution systems can be set to simulate a metastable state (aqueous phase) or stable state (aqueous and solid phase). Studies have shown that the forward mode is less affected by instrument measurement errors than the reverse mode (Ding et al., 2019;Song et al., 2018). Additionally, the minimum average RH of about 55% was recorded during the sampling period at the ten sites. Thus, ISORROPIA-II was run in the forward model for the aerosol system in the metastable condition and only used data with RH ≥ 30% for simulation accuracy (Ding et al., 2019;Song et al., 2018). The ISORROPIA model calculated the particle hydrate ion concentration per volume of air ($H_{air}^{+}$) and aerosol water associated with inorganic matter ($AWC_{inorg}$). The pH value was calculated using the following equation (Bougiatioti et al., 2016):

$$pH = -\log_{10} H_{aq}^{+} = -\log_{10} \frac{1000 H_{air}^{+}}{AWC_{inorg} + AWC_{org}} \quad (2.1)$$

where the modeled concentrations for $AWC_{inorg}$ and $H_{air}^{+}$ are μg/m$^3$, and $AWC_{org}$ is the particle water associated with the organic matters predicted using the following method:

$$AWC_{org} = \frac{m_s}{\rho_s} \frac{k_{org}}{\left(\frac{1}{RH} - 1\right)} \quad (2.2)$$

where $m_s$ is the mass concentration of organic matter (OM = OC × *f*). The *f* is the conversion factor of OC, which is dependent on the extent of OM oxidation and secondary organic aerosol formation (Chow et al., 2015). Studies on the ratio of OM/OC in fourteen cities in China suggested that the mean value of *f* was 1.59 ± 0.18 during the winter season in Northern China (Xing et al., 2013), and thus we adopted 1.6 as the *f* in this study. $k_{org}$ is the organic hygroscopicity parameter and depends on organic functionality, water solubility, molecular weight, and oxidation level. Han et al. (2022) have reported that the $k_{org}$ generally increased with O: C ratios, with a range of 0–0.3 for 23 organics, including carboxylic acids, amino acids, sugars, and alcohols. Gunthe et al. (2011) estimated a $k_{org}$ = 0.06 ± 0.01 for the effective average hygroscopicity of the non-refractory organic particulate matter in the aerosols in Beijing. Our previous study has estimated that the uncertainties of $k_{org}$ value (0.06) for pH in the range of 0–0.3 only lead to −1–3% errors, which can be neglected (Wang et al., 2023a). Therefore, the value of 0.06 was selected in this paper. $\rho_s$ is the organic density, which was chosen to be 1.35 g/cm$^3$ following previous studies (Table S2).

### 2.3.2 The sources of HONO

The sources of HONO include direct emission ($P_{emi}$), the homogeneous reaction of NO and •OH ($P_{OH+NO}$), the heterogeneous reaction of $NO_2$ on the ground ($P_{ground}$) and aerosol ($P_{aerosol}$), the photo-enhanced heterogeneous reaction of $NO_2$ on the ground ($P_{ground+hv}$) and aerosol ($P_{aerosol+hv}$), and nitrate photolysis ($P_{nitrate}$). The detailed calculation method is described in the Supplementary Material (Text S4, Table S3, Figs. S2 and S3).

Soil emission has been demonstrated to be a major source of HONO, which is affected by temperature to some extent (Liu et al., 2020c;Liu et al., 2020b). However, during the sampling periods, there was no significant positive correlation between HONO concentration and temperature (Fig. S4). In addition, temperatures did not exceed 10°C, under which the soil HONO emission rate is generally considered to be zero (Zhang et al., 2023). Furthermore, the equilibrium gas-phase concentration over an aqueous solution of nitrous acid, [HONO]*, a key parameter controlling the exchange of HONO between the gas and aqueous phase in soil, is calculated according to Su et al.(2011). The results indicate that the temperature difference between PC and DC periods only led to approximately a 0.01% concentration change. On the other hand, studies on the sources of HONO in the North China Plain of China during winter consistently showed that soil HONO emissions contribute around 1% (Liu et al., 2020c;Liu et al., 2020b;Zhang et al., 2023). Therefore, this study does not consider soil HONO emissions.

### 2.3.3 Redox reaction of $NO_2$ with $SO_2$.

The redox reaction of $NO_2$ with $SO_2$ ($R_1$) is considered a crucial potential source of high concentrations of HONO in Northern China (Cheng et al., 2019;Wang et al., 2016):

$$S(IV) + 2NO_2 + H_2O \rightarrow S(VI) + 2H^+ + 2NO_2^- \quad (R_1)$$

the rate expression for reaction ($R_1$) was estimated to:

$$d[S(VI)] / dt = k_1[NO_2][S(VI)], \quad (2.3)$$

the rate constant $k_1$ value is pH dependent, e.g., for pH, 5, $k_1 = (1.4\times10^5+1.24\times10^7)/2$ $M^{-1}\ s^{-1}$. For $k_1$ values under other pH conditions and other related information, please refer to Text S5, Table S4, and Table S5.

# 3. Results and discussion

## 3.1 Variations of $NH_3$, $NH_4^+$ and $TNH_x$.

The temporal variations of $NH_3$, $NH_4^+$, and $TNH_x$ at 10 sampling sites in the pre-COVID-19 pandemic period (PC, January 1 to 23, 2020) and during the COVID-19 pandemic period (DC, January 24 to February 29, 2020) are presented in Fig. 1, with their average concentration listed in Table 1. In general, rural sites exhibited higher concentrations of $NH_3$, $NH_4^+$, and $TNH_x$ compared to urban sites, except for the R-NY site. This finding is consistent with previous studies conducted in Zhengzhou (Wang et al., 2020), Shanghai (Chang et al., 2019), and Quzhou (Feng et al., 2022), owing to the intense agricultural ammonia emissions. The highest concentrations of $NH_3$ and $TNH_x$ were recorded at site R-JZ, with average values of 25.3 ± 11.5 and 40.8 ± 20.1 μg/m$^3$, respectively. Site R-AY had the highest $NH_4^+$ concentration, measuring 19.3 ± 12.9 μg/m$^3$. Note that the current study area exhibited higher $NH_3$ levels compared to other regions (Table S6), which probably was attributed to the highest $NH_3$ emissions of Henan Province in China, primarily from nitrogen fertilizer application and livestock farming (Wang et al., 2018;Ma, 2020).

Compared to the PC, $NH_3$ concentrations increased in the DC at all sites. Notably, rural sites experienced more significant increases in $NH_3$ concentrations than urban sites, which was similar to the trend in Shanghai (Xu et al., 2022). The largest increases in $NH_3$ concentrations were observed at R-SQ (71%, 7.3 μg/m$^3$) and U-ZK (37%, 4.8 μg/m$^3$) for rural and urban sites, respectively. In contrast, the concentrations of $NH_4^+$

and $TNH_x$ decreased in the DC with the largest reduction at rural site R-PY (51%, 12.9 μg/m$^3$) and urban site U-ZMD (48%, 9.3 μg/m$^3$). Regarding $TNH_x$, rural sites exhibited larger reductions, with site R-SQ experiencing the largest decrease of 37% (4.7 μg/m$^3$).

Figure 2 illustrates the spatial distribution and the diurnal variation of $NH_3$ concentrations at the ten sites before and during the pandemic. $NH_3$ concentrations in most sites exhibited an unimodal trend in PC that $NH_3$ concentrations gradually increased after sunrise, reaching a peak around noon (11:00–12:00), and then decreased to a valley around 16:00–17:00. This diurnal pattern is similar to $NH_3$ variations observed in urban areas of Houston, USA, as a result of the natural emissions from vegetation and soil during photosynthesis (Gong et al., 2011). However, other studies have recorded a significant $NH_3$ peak during the early morning of 8:00–10:00 (Ellis et al., 2011;Meng et al., 2018;Gu et al., 2022), suggesting the influence of vehicle emissions (Gong et al., 2011;Gu et al., 2022), residual $NH_3$ mixing, soil or plant emissions (Ellis et al., 2011), and dew volatilization (Wentworth et al., 2016;Huang et al., 2021b). Therefore, the $NH_3$ in urban and rural areas of this study was probably less affected by $NH_3$ emissions from vehicles, different from the recent studies in megacities of China (e.g., Beijing and Shanghai) (Gu et al., 2022;Wu et al., 2023;Zhang et al., 2020b). In addition to the transport from agricultural emissions, urban $NH_3$ in this region might also originate from other non-agricultural sources, such as wastewater treatment, coal combustion, household waste, urban green spaces, and human excrement (Chang et al., 2019).

During the COVID-19 pandemic, the diurnal variation of $NH_3$ in both urban and rural sites still maintained an unimodal distribution. The peak values in urban sites remained consistent with PC levels, further demonstrating that the influence of vehicles on $NH_3$ in urban areas was limited. Notably, the peak time of $NH_3$ in rural sites shifted 1–2 hours earlier compared to the trend in PC. Ammonia in rural areas primarily originates from nitrogen fertilizer application, livestock, and poultry breeding (Feng et al., 2022;Meng et al., 2018), which are significantly influenced by T and RH (Liu et al., 2023). Table S7 and Fig. S5 reveal that there was an increased T and a decreased RH at rural sites in the DC than the PC, which could accelerate the evaporation of $NH_3$ and thus potentially lead to earlier peak $NH_3$ concentrations.

## 3.2 Gas-to-particle conversion of $NH_3$

The increased $NH_3$ accompanying decreased $NH_4^+$ in the DC suggests that the gas-particle partition of $NH_3$/ $NH_4^+$ may determine the elevated $NH_3$ concentrations. Meteorological parameters, including RH and T, play a crucial role in the gas-particle partitioning of $NH_3$ (Liu et al., 2023;Xu et al., 2020). Therefore, the higher T and lower RH in the DC (Table S7 and Fig. S5) favored the conversion of $NH_4^+$ to $NH_3$, resulting in a decrease in $\varepsilon(NH_4^+)$ ($[NH_4^+]/([NH_3] + [NH_4^+])$) compared to those in the PC (Table S7).

$NH_3$ primarily enters particles to neutralize acidic ions (Wang et al., 2020;Xu et al., 2020;Liu et al., 2017;Ye et al., 2011;Wells, 1998). Accordingly, the concentrations of required ammonia (Required-$NH_x$) and excess ammonia (Excess-$NH_x$) were calculated based on the acidic substances as follows (Wang et al., 2020):

$$\text{Required-NH}_x = 17 \times \left(\frac{[SO_4^{2-}]}{48} + \frac{[NO_3^-]}{63} + \frac{[Cl^-]}{35.5} + \frac{[HNO_3]}{64} + \frac{[HCl]}{36.5}\right) - 17 \times \left(\frac{[Na^+]}{23} + \frac{[K^+]}{39} + \frac{[Ca^{2+}]}{20} + \frac{[Mg^{2+}]}{12}\right) \tag{3.1}$$

$$\text{Excess-NH}_x = \text{TNH}_x - \text{Required-NH}_x \tag{3.2}$$

where [W] represents the concentration of the substance (μg/m$^3$). The significant linear fitting ($R^2$ is greater than 0.96, and the slope is close to 1) in Fig. S6 demonstrates that the anions and cations at each site were close to the equilibrium state. Therefore, the organic acids in $PM_{2.5}$ may have less effect on $NH_3$ and $NH_4^+$ and were not considered in Formula 3.1.

As shown in Fig. 3 and Table S8, compared to those in the PC, the concentration of Required-$NH_x$ in the DC significantly decreased (ranging from 37% at site R-JZ to 58% at site R-PY), while the concentration of Excess-$NH_x$ increased (ranging from 9% at site R-AY to 78% at site R-SQ). The reduction in the concentrations of sulfate and nitrate (Fig. S7) was responsible for the decrease in the concentration of Required-$NH_x$. To sum up, in addition to meteorological conditions, the substantial reduction in anthropogenic emissions of $SO_2$, $NO_x$, and other pollutants in the DC had led to a decrease in acidic substances (e.g., sulfate and nitrate) in particles, in turn, resulting in more gas-phase $NH_3$ concentration remaining in the atmosphere.

## 3.3 Particle pH before and during COVID-19

Diurnal patterns of particle pH in PC and DC at ten sites are summarized in Fig. 4 with their average values listed in Table S9. $PM_{2.5}$ shows consistent moderate acidity, with mean values in the range of 4.2–5.1, which were close to the values in previous studies (Table S9). Compared to the PC, the particle pH at ten sites increased obviously in the DC, with the highest increase of 0.5 (U-ZK) and 0.3 (R-PY) at urban and rural sites, respectively, which were the subject of an in-depth discussion in the following text.

To explore the dominant factors that determine the local particle pH level and result in the high pH during the DC, sensitivity tests of pH to chemical species (i.e., $TNH_x$, $TH_2SO_4$, $TNO_3$, TCl, TNa, $K^+$, $Ca^{2+}$, and $Mg^{2+}$) and meteorological parameters (i.e., T and RH) were performed. A given range for a variable (i.e., $TNH_x$) with corresponding average values of other parameters (i.e., $TH_2SO_4$, $TNO_3$, TCl, TNa, $K^+$, $Ca^{2+}$, $Mg^{2+}$, T, and RH) was input into the model and simulated to compare its effects on pH. As shown in Fig. S8, pH increases with the cation concentrations (i.e., $TNH_x$, $Na^+$, $K^+$, $Ca^{2+}$, and $Mg^{2+}$) increasing as well as the anion concentrations (i.e., $TH_2SO_4$, $TNO_3$, and $Cl^-$), T and RH decreasing. According to the average values of input data during PC (Blue line in Fig. S8) and DC (Red line in Fig. S8) at U-ZK and R-PY sites respectively, the changes in pH (ΔpH in Fig. 5) indicate that the decrease in $TNH_x$ concentration and the increase in T in DC led to a decrease in pH values (ΔpH: 0.09 at U-ZK and 0.08 at R-PY sites) compared to PC. However, this effect was outweighed by the decrease in $TH_2SO_4$ (ΔpH: 0.07 and 0.8 at U-ZK and R-PY sites, respectively) and $TNO_3$ (ΔpH: 0.05 and 0.4 at U-ZK and R-PY sites, respectively) concentrations as well as the increase in $K^+$ (ΔpH: 0.03 at U-ZK and 0.2 at R-PY site) and $Mg^{2+}$ (ΔpH: 0.01 at U-ZK and 0.04 at R-PY site) concentrations in the DC, and resulting in an overall increase in pH values in the DC. Furthermore, the relationship between particle pH with the concentrations of Required-$NH_x$, and Excess-$NH_x$, which considers all chemical components, is investigated to examine the dominant factor on the increasing pH in DC. As shown in Fig. 6, the higher Excess-$NH_x$ concentrations in the DC led to higher increases in pH values (ΔpH: 1 at U-ZK and 0.5 at R-PY site) than those in PC (ΔpH: 0.3 at U-ZK and 0.2 at R-PY site), thus Excess-$NH_x$ concentrations may be the key factor in promoting the pH values.

## 3.4 The influence of pH on HONO.

The observed HONO concentrations decreased by 18% and 54% at U-ZK (0.8 ppb) and R-PY (0.9 ppb) sites in the DC, respectively, compared to those (1.0 and 2.2 ppb) in the PC. Moreover, all the known HONO production sources rates including $P_{emi}$, $P_{OH+NO}$, $P_{ground}$, $P_{ground+hv}$, $P_{aerosol}$, $P_{aerosol+hv}$, and $P_{nitrate}$ (Fig. 7, Fig S9 and S10) show a decreasing trend from PC to DC, with the total reductions of 38% (from 30% to 45% in the scenario with the minimum and maximum uncertainty, respectively) and 79% (from 77% to 82% in the scenario with the minimum and maximum uncertainty, respectively) for U-ZK and R-PY, respectively. At the U-ZK, $P_{ground+hv}$ decreased the most (84%), while at the R-PY, $P_{nitrate}$ had the largest decrease about 85%, which was speculated to be related to the decrease of $NO_x$ and $NO_3^-$ concentration in DC. Note that the reduction rates in the overall known source and almost individual sources were greater than the reduction rates in HONO concentrations (Figs. 7 and 8), thus we hypothesized that there should be other sources capable of promoting HONO production.

There were positive correlations between HONO with $SO_2$, Excess-$NH_x$, $SO_4^{2-}$, and pH (Fig. S12) indicating that the $R_1$ reaction might form an amount of HONO and contribute to less reduction in the observed HONO concentrations. Considering that $R_1$ mainly reacts in the liquid phase, the calculated reaction rates of $R_1$ under the conditions of RH > 60% in the PC and DC periods are illustrated in Figs. 8 and S12. Despite the decrease in $NO_2$ and $SO_2$ concentrations in the DC, the increase in particle pH, increasing $HSO_3^-$ concentration in the aqueous phase, promoted the $R_1$ reaction rates by 58% and 59% at U-ZK and R-PY (Figure 8), respectively. Consequently, the enhanced $R_1$ reaction might prevent a large decrease in HONO (18% at U-ZK and 53% at R-PY) under the conditions of a significant reduction in vehicle emissions and a decline of 66% and 69% in $NO_2$ concentrations at U-ZK and R-PY, respectively.

## 3.5 Uncertainty

According to sensitivity tests of pH (Fig. S8) and $R_1$ (Fig. S12), pH increases with the concentrations of cations ($TNH_x$, TNa, $K^+$, $Ca^{2+}$, and $Mg^{2+}$) and OC increasing as well as anions ($TH_2SO_4$, $TNO_3$, and $Cl^-$) concentrations, T, and RH decreasing. $R_1$ reaction rate increases with the concentrations of AWC, $NO_2$, $SO_2$, pH, and pressure, while increasing as well as T decreasing. Therefore, two extreme scenarios (i.e., the maximum and minimum rate scenarios) were evaluated to estimate the uncertainty of pH, and $R_1$ based on the measurement uncertainties at the U-ZK and R-PY sites. Figure S13 suggests that the two extreme scenarios can lead to –10–7% and –71–125% uncertainties at the U-ZK site and –10–7% and –78–123% uncertainties at the R-PY site for pH and $R_1$, respectively. Even considering the above uncertainty in Fig. 8, it can still be observed that during the DC period, the decrease in HONO was less than that of $NO_2$, and the rate of the $R_1$ reaction increased.

Considering the conclusions of this study are based solely on observational data, there are certain limitations. For example, only the changes in the $R_1$ reaction of $PM_{2.5}$ were calculated, without considering variations in components, pH values, and $R_1$ reaction rates of coarse particles. Additionally, although this study selected scenarios with RH > 60% to calculate the $R_1$ reaction to ensure the presence of a liquid phase, it is evident that this approach overlooks some $R_1$ reactions. Furthermore, due to thermodynamic model calculations of pH values, changes in the mixed state of particle components, and the omission of organic acids, alongside the absence of gaseous $HNO_3$ and HCl in this study, these factors may lead to inaccuracies in pH value simulations and uncertainty in $R_1$ calculations(Pye et al., 2020;Haskins et al., 2018;Nah et al., 2018). Therefore, there is a certain degree of uncertainty in the conclusions regarding the growth of $R_1$ reactions in this paper. Nevertheless, by calculating the changes in $R_1$ reactions, this study provides a possible explanation for the relatively small decrease in HONO during the epidemic period.

# 4. Conclusions

Elevated $NH_3$ concentration was observed during the COVID-19 pandemic at both urban and rural sites in China. In addition to the rise in T and decrease in RH during the COVID-19 pandemic, which favored the conversion of $NH_4^+$ to $NH_3$, the significant decrease in sulfate and nitrate concentrations led to the decline in Required-$NH_x$ and was beneficial to the particle-phase $NH_4^+$ portioning to gas-phase $NH_3$. Furthermore, under the environmental conditions of increased anion concentrations (especially sulfate and nitrate) and increased cation concentrations, the pH values increased by 0.5

and 0.3 at U-ZK and R-PY sites increased during the pandemic, respectively. Consequently, the high pH values accelerated the formation rate of HONO through the oxidation-reduction reaction of $NO_2$ with $SO_2$ (an increase of 58% at U-ZK and 59% at R-PY, respectively), partially compensating for the decrease in HONO concentration caused by the decline in vehicle emissions, $NO_2$ and $NO_3^-$ concentrations during the COVID-19 pandemic.

# 5. Implications

HONO plays a crucial role as a precursor to OH radicals in the tropospheric atmosphere (Xue, 2022). There have been significant observations of high HONO concentrations in urban areas during the daytime, leading to a growing interest in understanding its sources in atmospheric chemistry (Jiang et al., 2022;Xu et al., 2019). The heterogeneous reaction mechanism of $NO_2$ on aerosol surfaces is currently the focus of research on HONO sources, particularly in regions with elevated levels of atmospheric particulate matter, where it could potentially become a major contributor to HONO production (Zhang et al., 2022;Liao et al., 2021b). One of the pathways for heterogeneous reactions on aerosol surfaces is the redox reaction of $NO_2$ with $SO_2$. However, the significance of this reaction in HONO production in the real atmosphere is often overlooked, as it relies on the high pH of aerosols (Ge et al., 2019). In recent years, there has been increasing attention on the enhancing effect of $NH_3$ on the redox reaction, with laboratory experiments demonstrating its ability to generate substantial amounts of HONO (Ge et al., 2019). This study highlights the importance of this reaction based on actual atmospheric observations. Furthermore, numerous studies have indicated that if control over $NH_3$ emissions continues to relax while $SO_2$ and $NO_2$ emissions decrease, the particle pH in future China is expected to rise steadily (Xie et al., 2020;Song et al., 2019;Wang et al., 2020). Consequently, the redox reaction of $NO_2$ with $SO_2$ could become a significant source of HONO in China. Therefore, it is crucial to coordinate the control of $SO_2$, $NO_x$, and $NH_3$ emissions to avoid a rapid increase in the particle pH.

**Data availability:** All the data presented in this article can be accessed through https://zenodo.org/records/10273539. (Zhang, 2023).

**Author contributions.** XZ Data Curation, Writing - Original Draft, Visualization. LW, NW, SM, and DZ Investigation, Visualization, Data Curation. DZ, HZ, and MW Investigation. SW Conceptualization, Data Curation, Supervision. RZ Data Curation, Funding acquisition. All people are involved in the discussion of the results.

**Competing interest.** The authors declare no competing financial interest.

**Acknowledgments.** This work was supported by the China Postdoctoral Science Foundation (2023M733220), the Zhengzhou $PM_{2.5}$ and $O_3$ Collaborative Control and Monitoring Project (20220347A), and the National Key Research and Development Program of China (No. 2017YFC0212403).

# References


Alicke, B.: OH formation by HONO photolysis during the BERLIOZ experiment, J. Geophy. Res., 108, 8247, https://doi.org/10.1029/2001JD000579, 2003.

Atkinson, R., Baulch, D.L., Cox, R.A., Crowley, J.N., Hampson, R.F., Hynes, R.G., Jenkin, M.E., and Rossi, M. J., Troe, J.: Evaluated kinetic and photochemical data for atmospheric chemistry: volume I - gas phase reactions of $O_x$, $HO_x$, $NO_x$ and $SO_x$ species., Atmos. Chem. Phys., 4,1461–1738, https://doi.org/10.5194/acp-4-1461-2004, 2004.

Bougiatioti, A., Nikolaou, P., Stavroulas, I., Kouvarakis, G., Weber, R., Nenes, A., Kanakidou, M., and Mihalopoulos, N.: Particle water and pH in the eastern Mediterranean: source variability and implications for nutrient availability, Atmos. Chem. Phys., 16, 4579–4591, https://doi.org/10.5194/acp-16-4579-2016, 2016.

Chang, Y., Zou, Z., Zhang, Y., Deng, C., Hu, J., Shi, Z., Dore, A. J., and Collett, J. L., Jr.: Assessing contributions of agricultural and nonagricultural emissions to atmospheric ammonia in a Chinese megacity. Environ. Sci. Technol., 53, 1822–1833., https://doi.org/10.1021/acs.est.8b05984, 2019.

Chen, X., Walker, J. T., and Geron, C.: Chromatography related performance of the monitor for aerosols and gases in ambient air (MARGA): laboratory and field-based evaluation. Atmos. Meas. Tech., 10, 3893–3908. https://doi.org/10.5194/amt-10-3893-2017, 2017.

Cheng, Y., Zheng, G., Wei, C., Mu, Q., Zheng, B., Wang, Z., Gao, M., Z., Q., He, K., Carmichael, G., Pöschl, U., and Su, and H.: Reactive nitrogen chemistry in aerosol water as a source of sulfate during haze events in China, Sci. Adv., 2, e1601530., https://doi.org/10.1126/sciadv.1601530, 2019.

Chow, J. C., Lowenthal, D. H., Chen, L. W. A., Wang, X., and Watson, J. G.: Mass reconstruction methods for $PM_{2.5}$: a review, Air Qual. Atmos. Health., 8, 243 – 263, https://doi.org/10.1007/s11869-015-0338-3, 2015.

Ding, J., Zhao, P., Su, J., Dong, Q., Du, X., and Zhang, Y.: Aerosol pH and its driving factors in Beijing, Atmos. Chem. Phys., 19, 7939–7954., https://doi.org/10.5194/acp-19-7939-2019, 2019.

Ellis, R. A., Murphy, J. G., Markovic, M. Z., VandenBoer, T. C., Makar, P. A., Brook, J., and Mihele, C.: The influence of gas-particle partitioning and surface-atmosphere exchange on ammonia during BAQS-Met, Atmos. Chem. Phys., 11, 133–145., https://doi.org/10.5194/acp-11-133-2011, 2011.

Feng, S., Xu, W., Cheng, M., Ma, Y., Wu, L., Kang, J., Wang, K., Tang, A., Collett, J. L., Fang, Y., Goulding, K., Liu, X., and Zhang, F.: Overlooked nonagricultural and wintertime agricultural $NH_3$ emissions in Quzhou county, north China plain: evidence from $^{15}N$-Stable Isotopes. Environ. Sci. Technol. Lett., 9, 127–133, https://doi.org/10.1021/acs.estlett.1c00935, 2022a.

Feng, T., Zhao, S., Liu, L., Long, X., Gao, C., and Wu, N.: Nitrous acid emission from soil bacteria and related environmental effect over the North China Plain, Chemos., 287, https://doi.org/10.1016/j.chemosphere.2021.132034, 2022b.

Fountoukis, C., Nenes, A.: ISORROPIA II: a computationally efficient thermodynamic equilibrium model for $K^+$-$Ca^{2+}$-$Mg^{2+}$-$NH_4^+$-$Na^+$-$SO_4^{2-}$-$NO^{3-}$-$Cl^-$-$H_2O$ aerosols. Atmos. Chem. Phys., 7, 4639–4659, https://doi.org/10.5194/acp-7-4639-2007, 2007.

Ge, S., Wang, G., Zhang, S., Li, D., and Zhang, H.: Abundant $NH_3$ in China enhances atmospheric HONO production by promoting the heterogeneous reaction of $SO_2$ with $NO_2$. Environ. Sci. Technol., 53, 14339–14347, https://doi.org/10.1021/acs.est.9b04196, 2019.

Gong, L., Lewicki, R., Griffin, R. J., Flynn, J. H., Lefer, B. L., and Tittel, F. K.: Atmospheric ammonia measurements in Houston, TX using an external-cavity quantum cascade laser-based sensor, Atmos. Chem. Phys., 11, 9721–9733, https://doi.org/10.5194/acp-11-9721-2011, 2011.

Gu, M., Pan, Y., Walters, W. W., Sun, Q., Song, L., Wang, Y., Xue, Y., and Fang, Y.: ehicular emissions enhanced ammonia concentrations in winter mornings: insights from diurnal nitrogen isotopic signatures. Environ. Sci. Technol., 56, 1578–1585, https://doi.org/10.1021/acs.est.1c05884, 2022.

Gunthe, S. S., Rose, D., Su, H., Garland, R. M., Achtert, P., Nowak, A., Wiedensohler, A., Kuwata, M., Takegawa, N., Kondo, Y., Hu, M., Shao, M., Zhu, T., Andreae, M. O., and Pöschl, U.: Cloud condensation nuclei (CCN) from fresh and aged air pollution in the megacity region of Beijing, Atmos. Chem. Phys., 11, 11023–11039, https://doi.org/10.5194/acp-11-11023-2011, 2011.

Han, S., Hong, J., Luo, Q., Xu, H., Tan, H., Wang, Q., Tao, J., Zhou, Y., Peng, L., He, Y., Shi, J., Ma, N., Cheng, Y., and Su, H.: Hygroscopicity of organic compounds as a function of organic functionality, water solubility, molecular weight, and oxidation level, Atmos. Chem. Phys., 22, 3985–4004, https://doi.org/10.5194/acp-22-3985-2022, 2022.

Haskins, J. D., Jaeglé, L., Shah, V., Lee, B. H., Lopez‐Hilfiker, F. D., Campuzano‐Jost, P., Schroder, J. C., Day, D. A., Guo, H., Sullivan, A. P., Weber, R., Dibb, J., Campos, T., Jimenez, J. L., Brown, S. S., and Thornton, J. A.: Wintertime gas‐particle partitioning and speciation of inorganic chlorine in the lower troposphere over the northeast united states and coastal ocean, J. Geophys. Res.: Atmos., 123, https://10.1029/2018jd028786, 2018.

Huang, X., Ding, A., Gao, J., Zheng, B., Zhou, D., Qi, X., Tang, R., Wang, J., Ren, C., Nie, W., Chi, X., Xu, Z., Chen, L., Li, Y., Che, F., Pang, N., Wang, H., Tong, D., Qin, W., Cheng, W., Liu, W., Fu, Q., Liu, B., Chai, F., Davis, S. J., Zhang, Q., and He, K.: Enhanced secondary pollution offset reduction of primary emissions during COVID-19 lockdown in China, Natl. Sci. Rev., 8, nwaa137, https://doi.org/10.1093/nsr/nwaa137, 2021a.

Huang, X., Zhang, J., Zhang, W., Tang, G., and Wang, Y.: Atmospheric ammonia and its effect on $PM_{2.5}$ pollution in urban Chengdu, Sichuan Basin, China. Environ. Pollut., 291, 118–195. https://doi.org/10.1016/j.envpol.2021.118195, 2021b.

Jiang, Y., Xue, L., Shen, H., Dong, C., Xiao, Z., and Wang, W.: Dominant processes of HONO derived from multiple field observations in contrasting environments. Environ. Sci. Technol. Lett., 9, 258–264, https://doi.org/10.1021/acs.estlett.2c00004, 2022.

Kleffmann, J., Gavriloaiei, T., Hofzumahaus, A., Holland, F., Koppmann, R., Rupp, L., Schlosser, E., Siese, M., and Wahner, A.: Daytime formation of nitrous acid: A major source of OH radicals in a forest, Geophys. Res. Lett., 32, https://doi.org/10.1029/2005gl022524, 2005.

Kramer, L. J., Crilley, L. R., Adams, T. J., Ball, S. M., Pope, F. D., and Bloss, W. J.: Nitrous acid (HONO) emissions under real-world driving conditions from vehicles in a UK road tunnel, Atmos. Chem. Phys., 20, 5231–5248, https://doi.org/10.5194/acp-20-5231-2020, 2020.

Li, J., An, X., Cui, M., Sun, Z., Wang, C., and Li, Y.: Simulation study on regional atmospheric oxidation capacity and precursor sensitivity, Atmos. Environ., 263, 118657, https://doi.org/10.1016/j.atmosenv.2021.118657, 2021a.

Li, S., Song, W., Zhan, H., Zhang, Y., Zhang, X., Li, W., Tong, S., Pei, C., Wang, Y., Chen, Y., Huang, Z., Zhang, R., Zhu, M., Fang, H., Wu, Z., Wang, J., Luo, S., Fu, X., Xiao, S., Huang, X., Zeng, J., Zhang, H., Chen, D., Gligorovski, S., Ge, M., George, C., and Wang, X.: Contribution of vehicle emission and $NO_2$ surface conversion to nitrous acid (HONO) in urban environments: implications from tests in a tunnel. Environ. Sci. Technol., 55, 15616–15624, https://doi.org/10.1021/acs.est.1c00405, 2021.

Liao, S., Zhang, J., Yu, F., Zhu, M., Liu, J., Ou, J., Dong, H., Sha, Q., Zhong, Z., Xie, Y., Luo, H., Zhang, L., and Zheng, J.: High gaseous nitrous acid (HONO) emissions from light-duty diesel vehicles. Environ. Sci. Technol., 55, 200–208, https://doi.org/10.1021/acs.est.0c05599, 2021.

Liu, J., Deng, H., Lakey, P. S. J., Jiang, H., Mekic, M., Wang, X., Shiraiwa, M., and Gligorovski, S.: Unexpectedly high indoor HONO concentrations associated with photochemical $NO_2$ transformation on glass windows. Environ. Sci. Technol., 54, 15680–15688, https://doi.org/10.1021/acs.est.0c05624, 2020a.

Liu, M., Song, Y., Zhou, T., Xu, Z., Yan, C., Zheng, M., Wu, Z., Hu, M., Wu, Y., and Zhu, T.: Fine particle pH during severe haze episodes in northern China. Geophys. Res. Lett., 44, 5213–5221, https://doi.org/10.1002/2017gl073210, 2017.

Liu, P., Chen, H., Song, Y., Xue, C., Ye, C., Zhao, X., Zhang, C., Liu, J., and Mu, Y.: Atmospheric ammonia in the rural North China Plain during wintertime: variations, sources, and implications for HONO heterogeneous formation. Sci. Total. Environ., 861, 160768, https://doi.org/10.1016/j.scitotenv.2022.160768, 2023.

Liu, Y., Ni, S., Jiang, T., Xing, S., Zhang, Y., Bao, X., Feng, Z., Fan, X., Zhang, L., and Feng, H.: Influence of Chinese New Year overlapping COVID-19 lockdown on HONO sources in Shijiazhuang, Sci. Total Environ., 745, 141025, https://doi.org/10.1016/j.scitotenv.2020.141025, 2020b.

Liu, Y., Zhang, Y., Lian, C., Yan, C., Feng, Z., Zheng, F., Fan, X., Chen, Y., Wang, W., Chu, B., Wang, Y., Cai, J., Du, W., Daellenbach, K. R., Kangasluoma, J., Bianchi, F., Kujansuu, J., Petäjä, T., Wang, X., Hu, B., Wang, Y., Ge, M., He, H., and Kulmala, M.: The promotion effect of nitrous acid on aerosol formation in wintertime in Beijing: The possible contribution of traffic-related emissions, Atmos. Chem. Phys., 20, 13023–13040, https://doi.org/10.5194/acp-20-13023-2020, 2020c.

Liu, Z., Wang, Y., Costabile, F., Amoroso, A., Zhao, C., Huey, L. G., Stickel, R., Liao, J., and Zhu, T.: Evidence of aerosols as a media for rapid daytime HONO production over China, Environ. Sci. Technol., 48, 13023–13040, https://doi.org/10.1021/es504163z, 2014.

Lu, K., Guo, S., Tan, Z., Wang, H., Shang, D., Liu, Y., Li, X., Wu, Z., Hu, M., and Zhang, Y.: Exploring atmospheric free-radical chemistry in China: the self-cleansing capacity and the formation of secondary air pollution, Natl. Sci. Rev., 6, 579-594, https://doi.org/10.1093/nsr/nwy073, 2018.

Luo, L., Bai, X., Lv, Y., Liu, S., Guo, Z., Liu, W., Hao, Y., Sun, Y., Hao, J., Zhang, K., Zhao, H., Lin, S., Zhao, S., Xiao, Y., Yang, J., and Tian, H.: Exploring the driving factors of haze events in Beijing during Chinese New Year holidays in 2020 and 2021 under the influence of COVID-19 pandemic, Sci. Total Environ., 859, 160172, https://doi.org/10.1016/j.scitotenv.2022.160172, 2023.

Ma, S.: High-resolution assessment of ammonia emissions in China: Inventories, driving forces and mitigation, Atmos. Environ., 229, https://doi.org/10.1016/j.atmosenv.2020.117458, 2020.

McFall, A. S., Edwards, K. C., and Anastasio, C.: Nitrate photochemistry at the air-ice interface and in other ice reservoirs, Environ. Sci. Technol., 52, 5710–5717, https://doi.org/10.1021/acs.est.8b00095, 2018.

Meng, Z., Xu, X., Lin, W., Ge, B., Xie, Y., Song, B., Jia, S., Zhang, R., Peng, W., Wang, Y., Cheng, H., Yang, W., and Zhao, H.: Role of ambient ammonia in particulate ammonium formation at a rural site in the North China Plain, Atmos. Chem. Phys., 18, 167–184, https://doi.org/10.5194/acp-18-167-2018, 2018.

Meusel, H., Tamm, A., Kuhn, U., Wu, D., Leifke, A. L., Fiedler, S., Ruckteschler, N., Yordanova, P., Lang-Yona, N., Pöhlker, M., Lelieveld, J., Hoffmann, T., Pöschl, U., Su, H., Weber, B., and Cheng, Y.: Emission of nitrous acid from soil and biological soil crusts represents an important source of HONO in the remote atmosphere in Cyprus, Atmos. Chem. Phys., 18, 799–813, https://doi.org/10.5194/acp-18-799-2018, 2018.

Nah, T., Guo, H., Sullivan, A. P., Chen, Y., Tanner, D. J., Nenes, A., Russell, A., Ng, N. L., Huey, L. G., and Weber, R. J.: Characterization of aerosol composition, aerosol acidity, and organic acid partitioning at an agriculturally intensive rural southeastern US site, Atmos. Chem. Phys., 18, 11471–11491, https://10.5194/acp-18-11471-2018, 2018.

Oswald, R., Behrendt, T., Ermel, M., Wu, D., Su, H., Cheng, Y., Breuninger, C., Moravek, A., Mougin, E., Delon, C., Loubet, B., Pommerening-Roser, A., Sorgel, M., Poschl, U., and Hoffmann, T., Andreae, M.O., Meixner, F.X., Trebs, I.: HONO emissions from soil bacteria as a major source of atmospheric reactive nitrogen., Science, 341, 1233–1235, https://www.science.org/doi/10.1126/science.1242266, 2013.

Pagsberg, P., Bjergbakke, E., Ratajczak, E., Sillesen, A.: Kinetics of the gas phase reaction OH + NO (+M)$^-$ > HONO (+M) and the determination of the UV absorption cross sections of HONO., Chem. Phys. Lett., 272, 383–390, https://doi.org/10.1016/s0009-2614(97)00576-9, 1997.

Platt, U., Perner, D., Harris, G. W., Winer, A. M., and Pitts, J. N.: Observations of nitrous acid in an urban atmosphere by differential optical absorption, Nature, 285, 312–314, https://doi.org/10.1038/285312a0, 1980.

Pye, H. O. T., Nenes, A., Alexander, B., Ault, A. P., Barth, M. C., Clegg, S. L., Collett Jr, J. L., Fahey, K. M., Hennigan, C. J., Herrmann, H., Kanakidou, M., Kelly, J. T., Ku, I. T., McNeill, V. F., Riemer, N., Schaefer, T., Shi, G., Tilgner, A., Walker, J.

T., Wang, T., Weber, R., Xing, J., Zaveri, R. A., and Zuend, A.: The acidity of atmospheric particles and clouds, Atmos. Chem. Phys., 20, 4809–4888, https://10.5194/acp-20-4809-2020, 2020.

Romer, P. S., Wooldridge, P. J., Crounse, J. D., Kim, M. J., Wennberg, P. O., Dibb, J. E., Scheuer, E., Blake, D. R., Meinardi, S., Brosius, A. L., Thames, A. B., Miller, D. O., Brune, W. H., Hall, S. R., Ryerson, T. B., and Cohen, R. C.: Constraints on aerosol nitrate photolysis as a potential source of HONO and $NO_x$. Environ. Sci. Technol., 52, 13738–13746, https://doi.org/10.1021/acs.est.8b03861, 2018.

Scharko, N. K., Berke, A. E., and Raff, J. D.: Release of nitrous acid and nitrogen dioxide from nitrate photolysis in acidic aqueous solutions, Environ. Sci. Technol., 48, 11991–12001, https://doi.org/10.1021/es503088x, 2014.

Shi, Q., Tao, Y., Krechmer, J. E., Heald, C. L., Murphy, J. G., Kroll, J. H., and Ye, Q.: Laboratory investigation of renoxification from the photolysis of inorganic particulate nitrate, Environ. Sci. Technol., 55, 854–861, https://doi.org/10.1021/acs.est.0c06049, 2021.

Song, S., Gao, M., Xu, W., Shao, J., Shi, G., Wang, S., Wang, Y., Sun, Y., and McElroy, M. B.: Fine-particle pH for Beijing winter haze as inferred from different thermodynamic equilibrium models, Atmos. Chem. Phys., 18, 7423–7438, https://doi.org/10.5194/acp-18-7423-2018, 2018.

Song, S., Nenes, A., Gao, M., Zhang, Y., Liu, P., Shao, J., Ye, D., Xu, W., Lei, L., Sun, Y., Liu, B., Wang, S., and McElroy, M. B.: Thermodynamic modeling suggests declines in water uptake and acidity of inorganic aerosols in Beijing winter haze events during 2014/2015–2018/2019. Environ. Sci. Technol. Lett., 6, 752–760, https://doi.org/10.1021/acs.estlett.9b00621, 2019.

Spataro, F., and Ianniello, A.: Sources of atmospheric nitrous acid: state of the science, current research needs, and future prospects, J. Air. Waste. Manag. Assoc., 64, 1232–1250, https://doi.org/10.1080/10962247.2014.952846, 2014.

Stieger, B., Spindler, G., van Pinxteren, D., Grüner, A., Wallasch, M., and Herrmann, H.: Development of an online-coupled MARGA upgrade for the 2 h interval quantification of low-molecular-weight organic acids in the gas and particle phases, Atmos. Meas. Tech. 12, 281–298, https://doi.org/10.5194/amt-12-281-2019, 2019.

Su, H., Cheng, Y., Oswald, R., Behrendt, T., Trebs, I., Meixner, F.X., Andreae, M.O., Cheng, P., and Zhang, Y., Poschl, U.: Soil nitrite as a source of atmospheric HONO and OH radicals., Science., 333, 1616–1618, https://doi.org/10.1126/science.1207687, 2011.

Twigg, M. M., Berkhout, A. J. C., Cowan, N., Crunaire, S., Dammers, E., Ebert, V., Gaudion, V., Haaima, M., Häni, C., John, L., Jones, M. R., Kamps, B., Kentisbeer, J., Kupper, T., Leeson, S. R., Leuenberger, D., Lüttschwager, N. O. B., Makkonen, U., Martin, N. A., Missler, D., Mounsor, D., Neftel, A., Nelson, C., Nemitz, E., Oudwater, R., Pascale, C., Petit, J.-E., Pogany, A., Redon, N., Sintermann, J., Stephens, A., Sutton, M. A., Tang, Y. S., Zijlmans, R., Braban, C. F., and Niederhauser, B.: Intercomparison of in situ measurements of ambient $NH_3$: instrument performance and application under field conditions, Atmos. Meas. Tech., 15, 6755–6787, https://doi.org/10.5194/amt-15-6755-2022, 2022.

Wang, C., Yin, S., Bai, L., Zhang, X., Gu, X., Zhang, H., Lu, Q., and Zhang, R.: High-resolution ammonia emission inventories with comprehensive analysis and evaluation in Henan, China, 2006–2016, Atmos. Environ., 193, 11–23, https://doi.org/10.1016/j.atmosenv.2018.08.063, 2018.

Wang, S., Wang, L., Li, Y., Wang, C., Wang, W., Yin, S., and Zhang, R.: Effect of ammonia on fine-particle pH in agricultural regions of China: comparison between urban and rural sites, Atmos. Chem. Phys., 20, 2719–2734, https://doi.org/10.5194/acp-20-2719-2020, 2020.

Wang, S., Wang, L., Fan, X., Wang, N., Ma, S., and Zhang, R.: Formation pathway of secondary inorganic aerosol and its influencing factors in Northern China: Comparison between urban and rural sites, Sci. Total Environ., 840, https://doi.org/10.1016/j.scitotenv.2022.156404, 2022.

Wang, S., Fan, X., Xu, Y., Zhang, R., and Ren, B.: Insight into the non-linear responses of particulate sulfate to reduced $SO_2$ concentration: A perspective from the aqueous-phase reactions in a megacity in Northern China, Atmos. Res., 290, https://doi.org/10.1016/j.atmosres.2023.106796, 2023a.

Wang, W., Wang, S., Xu, J., Zhou, R., Shi, C., and Zhou, B.: Gas-phase ammonia and $PM_{2.5}$ ammonium in a busy traffic area of Nanjing, China, Environ. Sci. Pollut. Res. Int., 23, 1691–1702, https://doi.org/10.1007/s11356-015-5397-3, 2016.

Wang, Y., Jin, X., Liu, Z., Wang, G., Tang, G., Lu, K., Hu, B., Wang, S., Li, G., An, X., Wang, C., Hu, Q., He, L., Zhang, F., and Zhang, Y.: Progress in quantitative research on the relationship between atmospheric oxidation and air quality, J.

Environ. Sci., 123, 350–366, https://doi.org/10.1016/j.jes.2022.06.029, 2023b.

Wells, M., Choularton, T. W., and Bower, K. N.: A modelling study of the interaction of ammonia with cloud., Atmos. Environ., 32, 359–363, https://doi.org/10.1016/s1352-2310(97)00199-4, 1998.

Wentworth, G. R., Murphy, J. G., Benedict, K. B., Bangs, E. J., and Collett Jr, J. L.: The role of dew as a night-time reservoir and morning source for atmospheric ammonia, Atmos. Chem. Phys., 16, 7435–7449, https://doi.org/10.5194/acp-16-7435-2016, 2016.

Wu, C., Lv, S., Wang, F., Liu, X., Li, J., Liu, L., Zhang, S., Du, W., Liu, S., Zhang, F., Li, J., Meng, J., and Wang, G.: Ammonia in urban atmosphere can be substantially reduced by vehicle emission control: A case study in Shanghai, China, J. Environ. Sci., 126, 754–760, https://doi.org/10.1016/j.jes.2022.04.043, 2023.

Xie, Y., Wang, G., Wang, X., Chen, J., Chen, Y., Tang, G., Wang, L., Ge, S., Xue, G., Wang, Y., and Gao, J.: Nitrate-dominated $PM_{2.5}$ and elevation of particle pH observed in urban Beijing during the winter of 2017. Atmos. Chem. Phys., 20, 5019–5033, https://doi.org/10.5194/acp-20-5019-2020, 2020.

Xing, L., Fu, T. M., Cao, J. J., Lee, S. C., Wang, G. H., Ho, K. F., Cheng, M. C., You, C. F., and Wang, T. J.: Seasonal and spatial variability of the OM/OC mass ratios and high regional correlation between oxalic acid and zinc in Chinese urban organic aerosols, Atmos. Chem. Phys., 13, 4307–4318, https://doi.org/10.5194/acp-13-4307-2013, 2013.

Xu, J., Chen, J., Zhao, N., Wang, G., Yu, G., Li, H., Huo, J., Lin, Y., Fu, Q., Guo, H., Deng, C., Lee, S.-H., Chen, J., and Huang, K.: Importance of gas-particle partitioning of ammonia in haze formation in the rural agricultural environment, Atmos. Chem. Phys., 20, 7259–7269, https://doi.org/10.5194/acp-20-7259-2020, 2020.

Xu, W., Kuang, Y., Zhao, C., Tao, J., Zhao, G., Bian, Y., Yang, W., Yu, Y., Shen, C., Liang, L., Zhang, G., Lin, W., and Xu, X.: $NH_3$-promoted hydrolysis of $NO_2$ induces explosive growth in HONO, Atmos. Chem. Phys., 19, 10557–10570, https://doi.org/10.5194/acp-19-10557-2019, 2019.

Xu, W., Zhao, Y., Wen, Z., Chang, Y., Pan, Y., Sun, Y., Ma, X., Sha, Z., Li, Z., Kang, J., Liu, L., Tang, A., Wang, K., Zhang, Y., Guo, Y., Zhang, L., Sheng, L., Zhang, X., Gu, B., Song, Y., Van Damme, M., Clarisse, L., Coheur, P. F., Collett, J. L., Jr., Goulding, K., Zhang, F., He, K., and Liu, X.: Increasing importance of ammonia emission abatement in $PM_{2.5}$ pollution control. Sci. Bull., 67, 1745–1749, https://doi.org/10.1016/j.scib.2022.07.021, 2022.

Xue, C.: Substantially growing interest in the chemistry of nitrous acid (HONO) in China: current achievements, problems, and future directions. Environ. Sci. Technol., 56, 7375–7377. https://doi.org/10.1021/acs.est.2c02237, 2022.

Ye, C., Zhang, N., Gao, H., and Zhou, X.: Photolysis of particulate nitrate as a source of HONO and $NO_x$. Environ. Sci. Technol., 51, 6849–6856, https://doi.org/10.1021/acs.est.7b00387, 2017.

Ye, X., Ma, Z., Zhang, J., Du, H., Chen, J., Chen, H., Yang, X., Gao, W., and Geng, F.: Important role of ammonia on haze formation in Shanghai, Environ. Res. Lett., 6, 024019, https://doi.org/10.1088/1748-9326/6/2/024019, 2011.

Zhang, Q., Liu, P., Wang, Y., Gerorge, C., Chen, T., Ma, S. L., Ren, Y., Mu, Y., Song, M., Herrmann, H., Mellouki, A., Chen, J., Zhao, X., Wang, S., and Y., Z.: Unveiling the underestimated direct emissions of nitrous acid (HONO), Proc. Natl. Acad. Sci. U.S.A., 120, https://doi.org/10.1073/pnas.2302048120, 2023.

Zhang, W., Tong, S., Jia, C., Wang, L., Liu, B., Tang, G., Ji, D., Hu, B., Liu, Z., Li, W., Wang, Z., Liu, Y., Wang, Y., and Ge, M.: Different HONO sources for three layers at the urban area of Beijing. Environ. Sci. Technol., 54, 12870–12880, https://doi.org/10.1021/acs.est.0c02146, 2020a.

Zhang, W., Tong, S., Jia, C., Ge, M., Ji, D., Zhang, C., Liu, P., Zhao, X., Mu, Y., Hu, B., Wang, L., Tang, G., Li, X., Li, W., and Wang, Z.: Effect of different combustion processes on atmospheric nitrous acid formation mechanisms: a winter comparative observation in urban, suburban and rural areas of the North China Plain. Environ. Sci. Technol., 56, 4828–4837, https://doi.org/10.1021/acs.est.1c07784, 2022.

Zhang, Y., Liu, X., Fang, Y., Liu, D., Tang, A., and Collett, J. L.: Atmospheric ammonia in Beijing during the COVID-19 outbreak: concentrations, sources, and implications. Environ. Sci. Technol. Lett., 8, 32–38, https://doi.org/10.1021/acs.estlett.0c00756, 2020b.

## Figures:

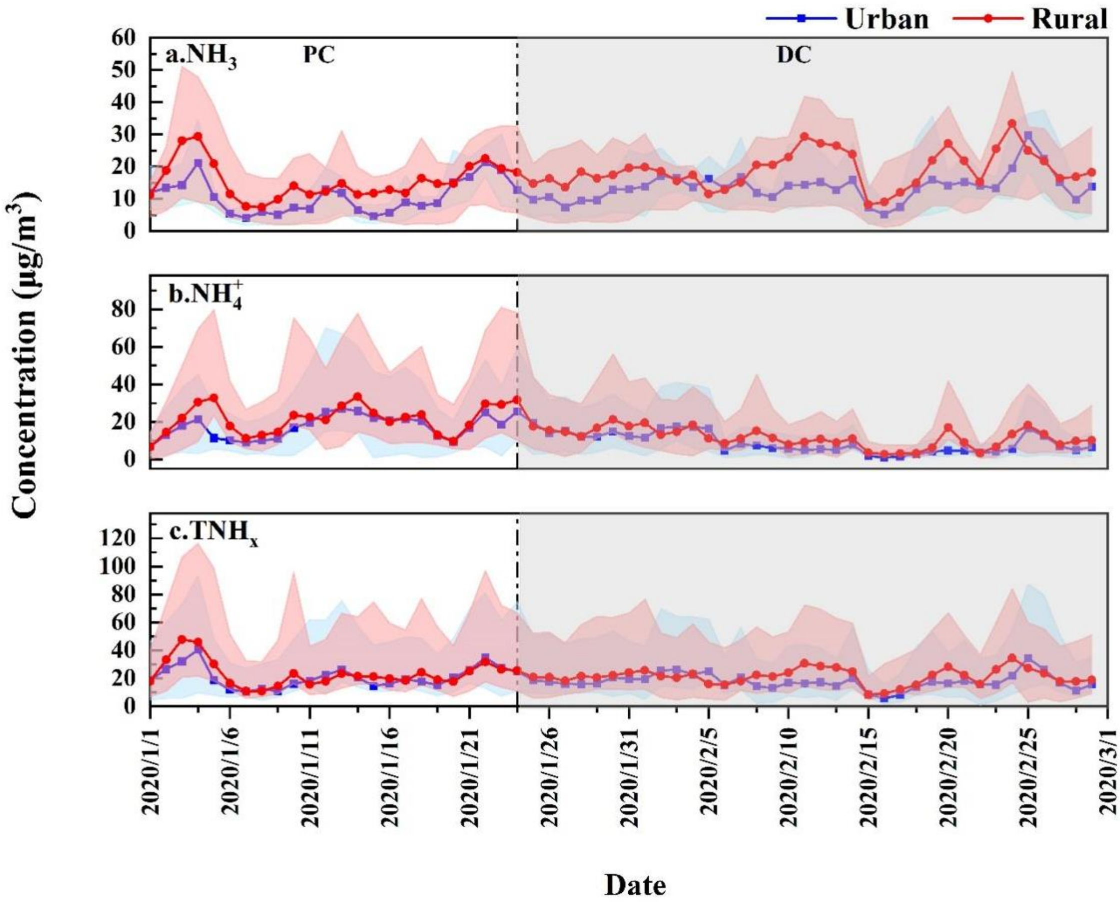


Figure 1. Temporal variations of a. $NH_3$, b. $NH_4^+$, and c. $TNH_x$ at the urban and rural sites before (PC) and during (DC) the COVID-19 outbreak, respectively. The shaded areas of the curve represent the maximum and minimum values.

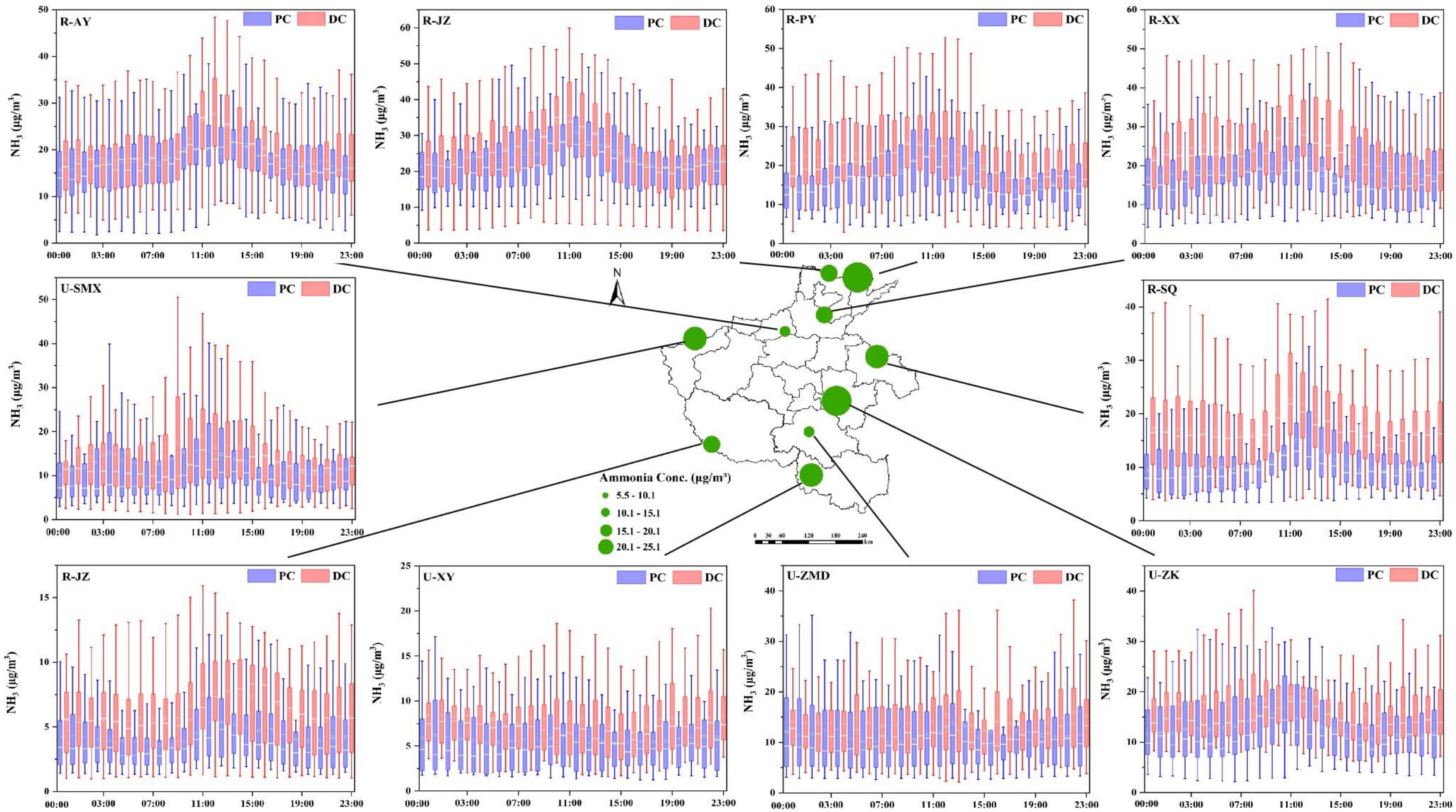


Figure 2. Daily variation of $NH_3$ concentrations at ten sites before (PC) and during (DC) the COVID-19 outbreak. The green dots represent the location of ten sites and their size represents the concentration of $NH_3$; In each box, the top, middle, and bottom lines represent the 75, 50, and 25 percentiles of statistical data, respectively; the upper and lower whiskers represent the 90 and 10 percentiles of statistical data, respectively.

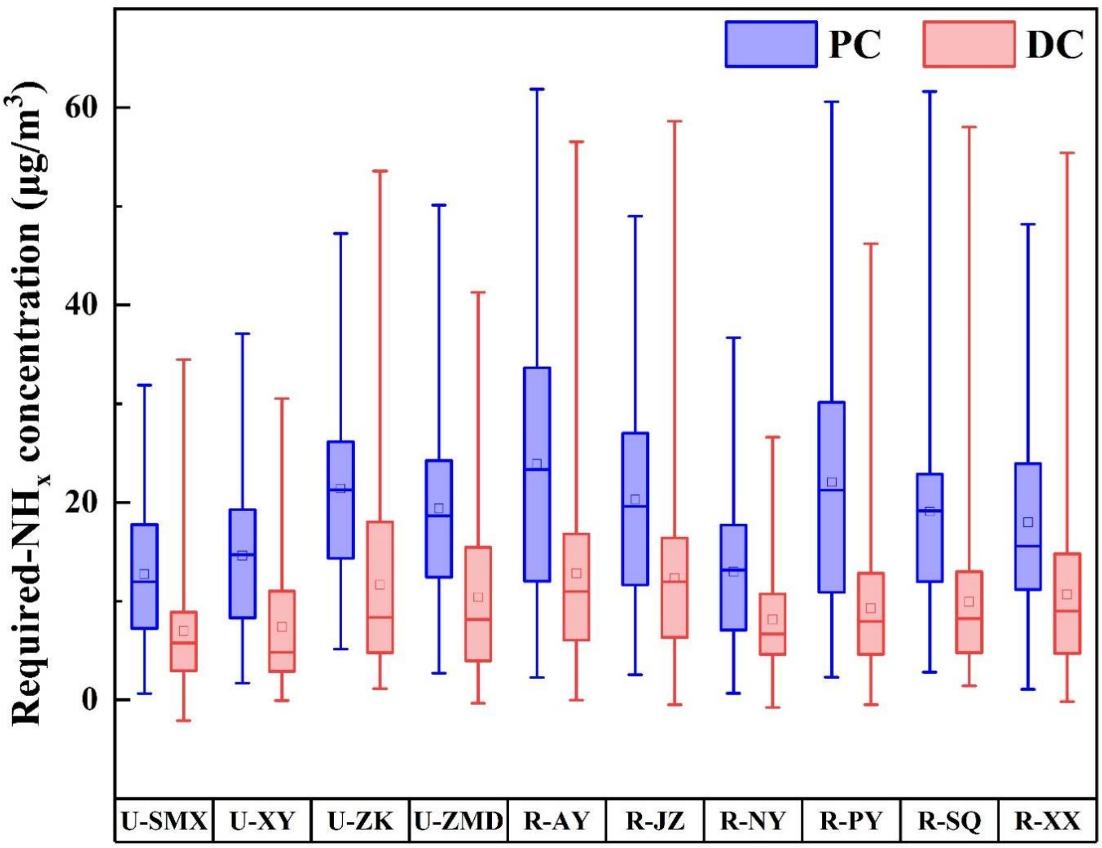


714

715 Figure 3. Box diagram of changes in Required-$NH_x$ at ten sites before (PC) and during
716 (DC) the COVID-19 outbreak. In each box, the top, middle, and bottom lines represent
717 the 75, 50, and 25 percentiles of statistical data, respectively; the upper and lower
718 whiskers represent the 90 and 10 percentiles of statistical data, respectively.

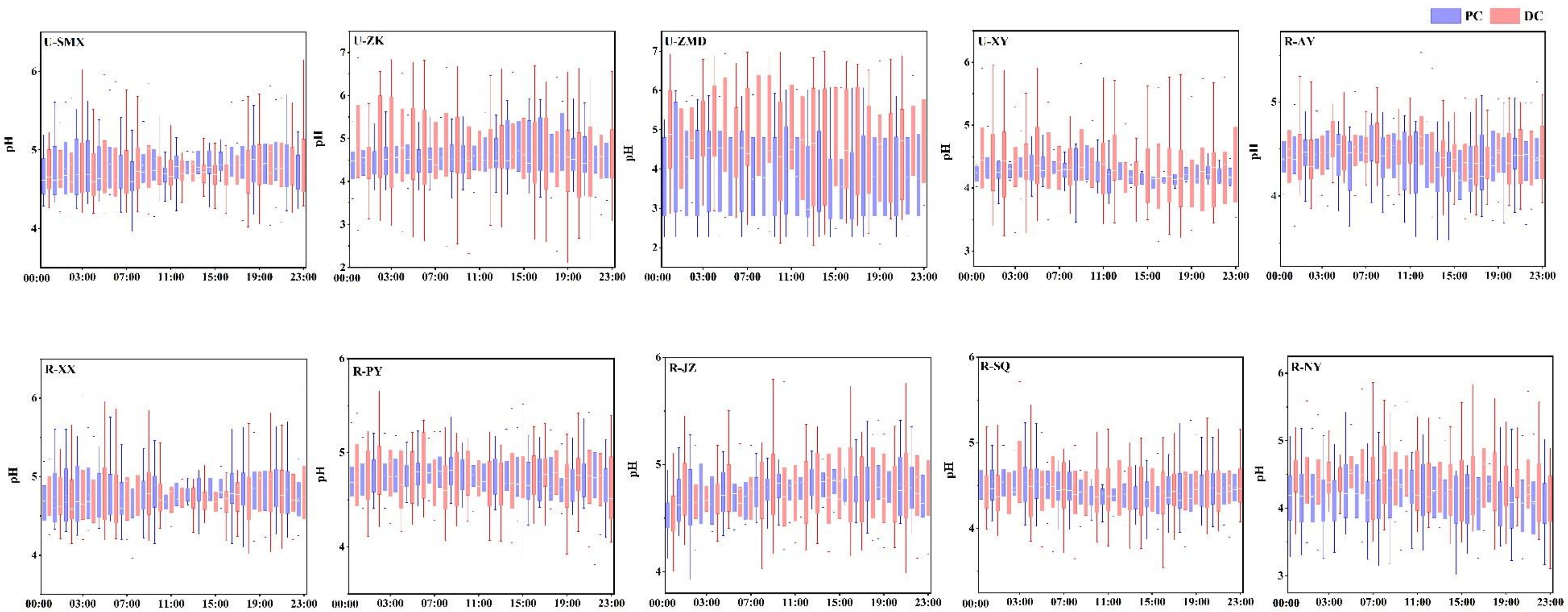


Figure 4. Diurnal patterns of pH at ten sites before (PC) and during (DC) the COVID-19 outbreak. In each box, the top, middle, and bottom lines represent the 75, 50, and 25 percentiles of statistical data, respectively; the upper and lower whiskers represent the 90 and 10 percentiles of statistical data, respectively.

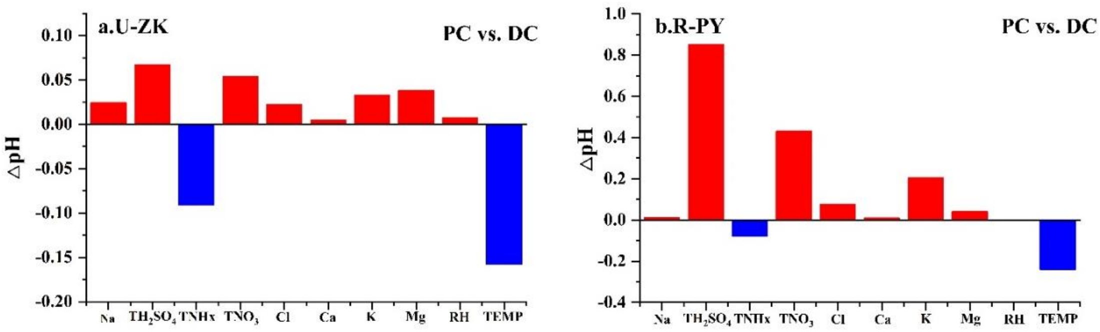


Figure 5. Changes of pH (ΔpH) through the sensitivity tests (Figure S5 and S6) by changing parameters between PC and DC at the a. U-ZK and b. R-PY sites.

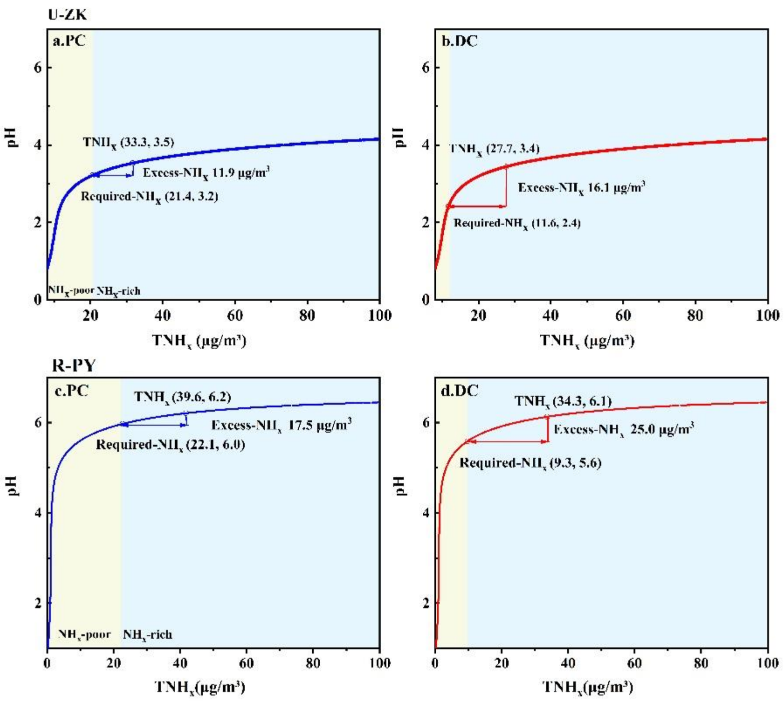


Figure 6. Particle pH corresponds to increasing $TNH_x$ at U-ZK and R-PY sites to examine the effects of major indicators of $NH_3$ (i.e., $TNH_x$, Required-$NH_x$, and Excess-$NH_x$) on aerosol acidity. Particle pH was calculated by using a wide range of $TNH_x$ (25–130 μg/m$^3$) and average values of other parameters in PC and DC of U-ZK and R-PY sites. The concentrations of $TNH_x$, Required-$NH_x$, and Excess-$NH_x$ with corresponding pH values are marked by a hollow box, hollow circle, and arrow respectively. The yellow and blue background colors correspond to the $NH_x$-poor and $NH_x$-rich, respectively.

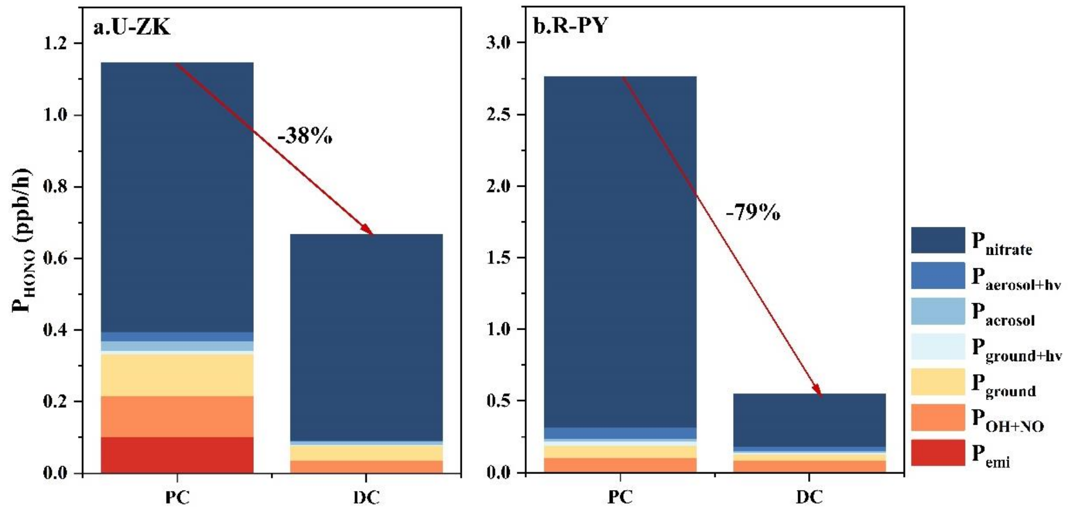


Figure 7. Comparison of HONO sources at a. U-ZK and b. R-PY sites before (PC) and during (DC) the COVID-19 outbreak. The calculation method can be found in Text S4.

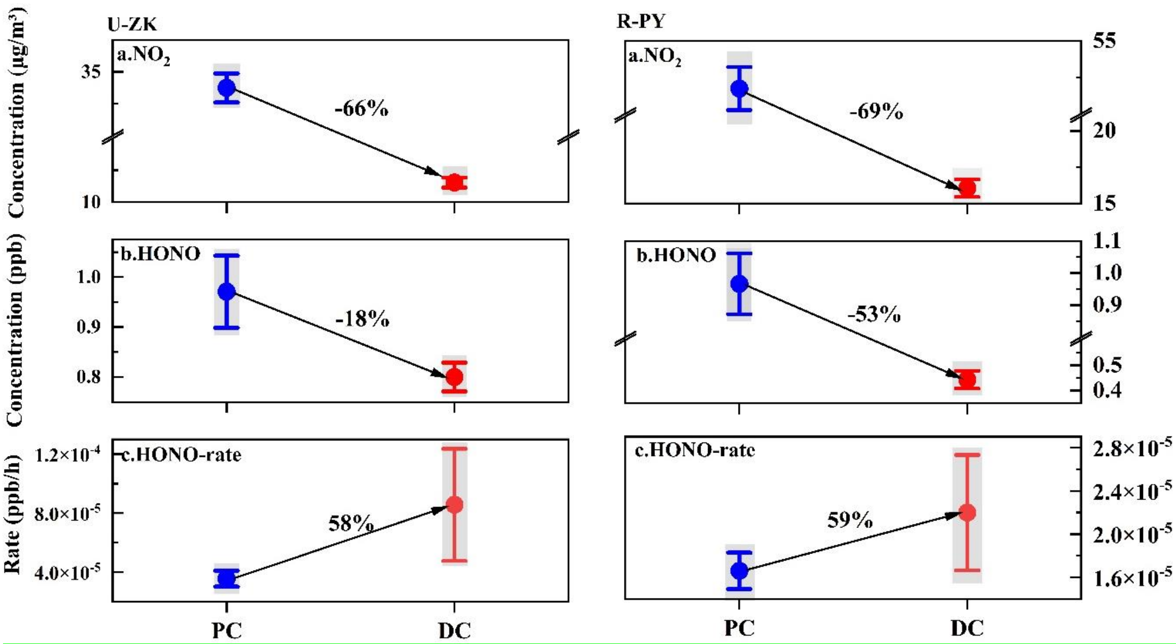


Figure 8. Decline ratios of a. $NO_2$, b. HONO concentration, and c. HONO production rate at U-ZK and R-PY sites before (PC) and during (DC) the COVID-19 outbreak. The center point represents the mean value, and the upper and lower whiskers represent the 95% confidence interval of the mean. The shadows in the figure represent the uncertainties of $NO_2$ measurement (±10%), HONO measurement (±20%), and the

HONO formation rate of $R_1$ reaction (–78–123%), respectively.

## Table:

Table 1. Changes in concentrations (mean ± standard deviation) of $NH_3$, $NH_4^+$, and $TNH_x$ at ten sites during entire periods (Average), before (PC), and during (DC) the COVID-19 outbreak.

| Sites | Substances | Average (μg/m³) | PC (μg/m³) | DC (μg/m³) |
|---|---|---|---|---|
| U-SMX | $NH_3$ | 13.8 ± 10.8 | 12.6 ± 10.1 | 14.5 ± 11.1 |
| | $NH_4^+$ | 10.9 ± 7.2 | 14.2 ± 7.2 | 8.8 ± 6.5 |
| | $TNH_x$ | 22.9 ± 14.1 | 24.9 ± 14.5 | 21.7 ± 13.8 |
| U-ZK | $NH_3$ | 15.6 ± 8.3 | 12.7 ± 6.5 | 17.4 ± 8.8 |
| | $NH_4^+$ | 13.6 ± 9.3 | 19.1 ± 8.4 | 10.3 ± 8.1 |
| | $TNH_x$ | 28.6 ± 13.7 | 30.9 ± 12.8 | 27.1 ± 14.0 |
| U-ZMD | $NH_3$ | 13.1 ± 8.4 | 11.6 ± 8.2 | 14.0 ± 8.4 |
| | $NH_4^+$ | 13.9 ± 9.8 | 19.6 ± 10.3 | 10.3 ± 7.5 |
| | $TNH_x$ | 25.7 ± 14.6 | 30.3 ± 15.1 | 22.8 ± 13.5 |
| U-XY | $NH_3$ | 7.0 ± 4.3 | 5.7 ± 4.0 | 7.9 ± 4.3 |
| | $NH_4^+$ | 11.0 ± 7.7 | 15.4 ± 7.6 | 8.3 ± 6.5 |
| | $TNH_x$ | 17.6 ± 9.8 | 20.6 ± 10.1 | 15.7 ± 9.2 |
| R-AY | $NH_3$ | 19.0 ± 8.4 | 17.9 ± 8.3 | 19.7 ± 8.4 |
| | $NH_4^+$ | 19.3 ± 12.9 | 26.4 ± 13.7 | 15.0 ± 10.3 |
| | $TNH_x$ | 36.6 ± 18.2 | 41.7 ± 20.4 | 33.4 ± 16.0 |
| R-XX | $NH_3$ | 21.7 ± 10.2 | 18.1 ± 9.3 | 23.8 ± 10.1 |
| | $NH_4^+$ | 15.9 ± 10.4 | 20.6 ± 11.0 | 13.0 ± 8.8 |
| | $TNH_x$ | 34.9 ± 17.0 | 35.1 ± 18.8 | 34.8 ± 15.8 |
| R-PY | $NH_3$ | 19.8 ± 9.4 | 16.8 ± 8.1 | 21.7 ± 9.6 |
| | $NH_4^+$ | 17.4 ± 11.8 | 25.3 ± 12.6 | 12.4 ± 8.0 |
| | $TNH_x$ | 35.2 ± 17.8 | 39.4 ± 19.8 | 32.6 ± 15.7 |
| R-JZ | $NH_3$ | 25.3 ± 11.5 | 24.1 ± 11.5 | 25.9 ± 11.4 |
| | $NH_4^+$ | 17.3 ± 11.3 | 22.7 ± 11.6 | 14.2 ± 9.9 |
| | $TNH_x$ | 40.8 ± 20.1 | 42.9 ± 22.8 | 33.5 ± 18.2 |
| R-SQ | $NH_3$ | 15.0 ± 7.9 | 10.3 ± 5.2 | 17.7 ± 7.9 |
| | $NH_4^+$ | 13.4 ± 8.5 | 18.9 ± 8.6 | 10.3 ± 6.7 |
| | $TNH_x$ | 26.3 ± 13.2 | 25.5 ± 14.0 | 26.8 ± 12.7 |
| R-NY | $NH_3$ | 5.5 ± 3.1 | 4.3 ± 2.7 | 6.2 ± 3.2 |
| | $NH_4^+$ | 10.2 ± 6.9 | 13.3 ± 7.2 | 8.4 ± 6.1 |
| | $TNH_x$ | 14.8 ± 8.5 | 16.0 ± 9.5 | 14.1 ± 7.8 |